# nature communications



**Article** 

https://doi.org/10.1038/s41467-025-62546-8

# Semitransparent organic photovoltaics with wide geographical adaptability as sustainable smart windows

Received: 6 March 2025

Accepted: 22 July 2025

Published online: 11 August 2025

Check for updates

Jiangsheng Yu <sup>1</sup>0 Jihong Pu<sup>2</sup>, Dongsheng Xie<sup>3</sup>, Zhenhai Ai<sup>1</sup>, Yongwen Lang<sup>1</sup>, Menghua Cao<sup>1</sup>, Chunhui Duan <sup>3</sup> ⊠, Lin Lu <sup>2</sup> ⊠ & Gang Li <sup>1,4</sup> ⊠

Semitransparent organic photovoltaics (ST-OPVs) have gained significant attention due to their rapid iteration of high-efficiency photoactive materials and potential applications in building-integrated photovoltaics as smart windows. In this work, we establish a parameter (FoM<sub>LUE</sub>) to evaluate the potential of photoactive materials for ST-OPVs, combining average visual transmittance, bandgap, and current density. PBOF and eC9 exhibit the highest FoM<sub>LUE</sub> values of 0.084 and 0.161 for the investigated donors and acceptors, respectively. We achieve a light utilization efficiency of 6.05% as the figure of merit for all semitransparent solar cells. The derived ST-OPV exhibits enhanced thermal insulation and operational stability compared to its counterpart. The geographical analysis indicates that the hot summer/warm winter zone is the most suitable for ST-OPV glazing windows, delivering an annual total energy-saving of 1.43 GJ m<sup>-2</sup>. Our results demonstrate the multifunctionality and geographical factors of ST-OPVs for constructing sustainable energy-saving smart windows.

Transparent solar cells have the potential to revolutionize the renewable energy sector, allowing them to be integrated into everyday objects such as windows, screens, and other surfaces, without obstructing the view or the design aesthetics<sup>1-4</sup>. There are challenges to overcome, including improving the efficiency and lifespan of the solar cells and reducing the cost of production. Transparent solar cells primarily absorb ultraviolet and infrared light, which are invisible to the human eye. This technology involves an inherent tradeoff between transparency and efficiency. Semitransparent organic photovoltaics (ST-OPVs) are arousing a passion for transparent research, due to their unique discrete absorption, low-cost production, and environmental friendliness<sup>5-8</sup>. The key advantage of ST-OPVs lies in their ability to combine energy generation with a visually appealing design. This feature opens up a range of applications, especially in the context of building-integrated

photovoltaics (BIPV), for example, solar windows without detracting from the architectural design°.

Overcoming challenges related to efficiency, aesthetic flexibility, stability, and integration will be crucial for unlocking the full potential of ST-OPVs in the BIPV market. Transparent solar cells are engineered to achieve maximum power conversion efficiency (PCE) while maintaining high average visual transmittance (AVT), thus light utilization efficiency (LUE), the product of PCE and AVT, severs as a critical figure of merit to benchmark their development. Recently, the PCEs of OPVs have been significantly improved, surpassing 20%, due to advancements in semiconducting materials and device engineering, especially the mushrooming non-fullerene small molecule acceptors (NFAs)<sup>10-13</sup>. These NFAs show strong absorption in the near-infrared (NIR) region up to 1000 nm. Normally, a wide bandgap polymer donor of about 1.8 eV is compositional as the high-performance active layer, such as

<sup>1</sup>Department of Electrical and Electronic Engineering, Research Institute for Smart Energy (RISE), Photonic Research Institute (PRI), The Hong Kong Polytechnic University, Hong Kong, China. <sup>2</sup>Department of Building Environment and Energy Engineering, The Hong Kong Polytechnic University, Hong Kong, China. <sup>3</sup>Institute of Polymer Optoelectronic Materials and Devices, Guangdong Basic Research Center of Excellence for Energy & Information Polymer Materials, State Key Laboratory of Luminescent Materials and Devices, South China University of Technology, Guangzhou, China. <sup>4</sup>Guangdong-Hong Kong-Macao Joint Laboratory for Photonic-Thermal-Electrical Energy Materials and Devices, Hong Kong Polytechnic University, Hong Kong, China.

e-mail: duanchunhui@scut.edu.cn; vivien.lu@polyu.edu.hk; gang.w.li@polyu.edu.hk

PM6<sup>14</sup>, PTQ10<sup>15</sup>, and PBQx-TF<sup>16</sup>. Whereas, the absorption spectra of these donors are highly coincident with the visible wavelength range (380–740 nm), resulting in a drastic decrease in the AVT. Reducing the proportion of the polymer donor is an effective means to regulate the absorption distribution of active layer, thus improving LUE values in derived ST-OPVs. For example, Chen et al. increased the selective absorption by tuning the PM6:acceptors ratio from 1:1.3 to 1:3, and achieved a high LUE of 5.0% with comprehensive optimizations, including the thicknesses of active layer and metal electrode, antireflection, etc<sup>17</sup>. Developing narrow or ultrawide bandgap polymer donors is also conducive to higher AVT for ST-OPVs<sup>18</sup>. Zhu et al. reported that PTB7-Th-based ST-OPVs exhibit superior see-through properties with a high AVT of 50.8%, where the ATT-9 acceptor with an optical response of over 1000 nm is utilized, and silver nanowires served as transparent top electrode<sup>19,20</sup>. While the narrow band gap polymer donor lowers open-circuit voltage  $(V_{OC})$ , leading to an inferior PCE in devices. Recently, we have achieved a LUE of 3.05% for ST-OPVs without optical modulation by employing an ultra-wide bandgap polymer donor named PBOF (2.20 eV), whose absorption shows minimal spectral overlap with the photopic response of human eve<sup>21</sup>. The top electrode is another critical factor for high-performance ST-OPVs. Metal, including ultrathin Ag and Au, silver nanowires, graphene, and conducting polymers, are the main categories as transparent top electrodes for ST-OPVs. All these materials do not possess selective absorption intrinsically. Our group has successfully constructed a superior transparent top electrode via integrating an aperiodic bandpass filter atop thin Ag, which exhibits a high AVT of about 80% and a total reflection in the 700-900 nm region<sup>22</sup>. Using this strategy, a record-breaking LUE of 5.35% has been achieved due to its remarkable enhancement in AVT without losing short-circuit density (I<sub>SC</sub>) compared with its counterpart without optical design.

Another key challenge in BIPV is ensuring that the photovoltaic system does not compromise the visual appeal of the building. The aesthetic flexibility of ST-OPVs can be adjusted in their transparency to meet both functional and aesthetic needs<sup>23-25</sup>. The visual aesthetics of ST-OPVs are evaluated based on two key metrics, the color rendering index (CRI) and Commission Internationale de L'Eclairage (CIE 1931) chromaticity coordinates, which together quantify the quality and color of the light that passes through the device. Optical manipulations are widely applied to tune the color perception of ST-OPVs<sup>26–28</sup>. The CIE chromaticity coordinates of neutral color and AM1.5 G are (0.333, 0.333) and (0.332, 0.343), respectively. Through neutral-colored ST-OPVs with a CRI close to 100, the object's color can appear as it is under natural light, strengthening the potential of power window application. CRI values above 90 are categorized as excellent. Considering the inherently visible absorption of organic active layers, optical modulation in terms of material selection and photonic structure has been demonstrated as an efficient path for adjusting the CRI of ST-OPVs. ST-OPVs can provide an added benefit by controlling the amount of natural light entering the building<sup>29</sup>. This feature allows for more efficient daylight harvesting and reduced reliance on artificial lighting, contributing to overall energy savings. The use of ST-OPVs in windows can help manage solar heat gain, contributing to better thermal regulation inside the building<sup>30-32</sup>. However, the power generation and energysaving performance of ST-OPV-based BIPV under different climates have been rarely reported. The impact of geographical factors, including ambient air temperature, latitude, altitude, and solar radiation intensity, on the application of the ST-OPV-based buildings has not been revealed. Thus, an optimal balance between the electrical and optical properties of ST-OPVs requires an in-depth investigation for further promoting commercialization prospects.

In this work, we screen a series of classic photoactive materials to investigate their selective absorption, such as P3HT<sup>33</sup>, PTB7-Th<sup>34</sup>, PM6, PTQ10, D18-Cl<sup>35</sup>, PBQx-TF, PBOF, PC61BM<sup>36</sup>, PC71BM<sup>37</sup>, L8-BO<sup>38</sup>, eC9<sup>39</sup>, eC9-2Cl<sup>16</sup>. We demonstrate a dimensionless parameter (FoM<sub>LUE</sub>) to

evaluate the potential of photoactive materials for ST-OPVs. The FoMILIE parameter takes into account three aspects, AVT, bandgap. and current density, through investigating the normalized absorbance of photoactive material. In three categories (polymer donors, fullerenes, NFAs), PBOF, PC61BM, and eC9 exhibit higher selective absorption than their counterparts, as evidenced by the calculated results of FoM<sub>LUE</sub> values. PBOF and eC9 exhibit the highest FoM<sub>LUE</sub> values of 0.084 and 0.161 for donor and acceptor, respectively. The calculated FoM<sub>LUE</sub> values imply its superior efficiency potential of PBOF: eC9: PC61BM (0.091) for ST-OPVs. The photovoltaic performance of PBOF: eC9: PC61BM based devices is finely characterized through the comprehensive optimization of the hole transport layer (HTL), composition, and additives, delivering the highest PCE of 18.60% with  $J_{SC}$  of 26.75 mA cm<sup>-2</sup>,  $V_{OC}$  of 0.884 V, and fill factor (FF) of 78.66%. Compared to its counterpart, the impacts of self-assembled monolayer (SAM) as HTL, 10% wt PC61BM as the third component, and solid additive on the photovoltaic performance are thoroughly explored through device physical analysis, morphological analysis, and energy loss analysis. ST-OPVs based on the optimal ternary (PBOF: eC9: PC61BM) blends with various thicknesses (50~120 nm) are explored with thin silver electrode (11 nm). The 60-nm ST-OPVs achieve the highest LUE of 4.12%. Attributed to the significantly increased AVT of 50.86% and 49.62%, the 40-nm tellurium dioxide (TeO<sub>2</sub>) and aperiodic band-pass filter (ABPF)-based ST-OPVs achieve PCEs of 10.47% and 12.19%, delivering LUEs of 5.32% and 6.05%, respectively. To our best knowledge, the LUE of 6.05% as the figure of merit for semitransparent solar cells is the highest value in the literature. The aesthetic transparency of these devices presents a reddish hue with high CRI values exceeding 90. Among the devices tested, the ABPF based ST-OPVs show the highest operational stability, with a  $T_{80}$ lifetime exceeding 800 h under continuous illumination. The thermal insulation performance of these ST-OPVs is quantified and qualified by setting up a prefabricated structure. Considering the power generation and thermal insulation capabilities, the ABPF based ST-OPVs exhibit multifunctional performance, revealing their promising potential in the field of BIPVs as smart windows. The transient model results indicate that the hot summer/warm winter zone is the most suitable for ST-OPVs as a double-glazed window across China, delivering an average annual energy-saving of 1.43 GJ m<sup>-2</sup>. Our results highlight the multifunctionality and the influence of geographical factors on the high-efficiency ST-OPVs, demonstrating their potential for applications in power generation and energy-saving BIPVs.

# **Results**

# The assessment parameter of FoM<sub>LUE</sub>

High-performance ST-OPVs depend on successfully managing the inherent trade-off between photovoltaic and optical transparency. Therefore, determining a parameter for photoactive material screen is vital. Herein, the formula combines three factors, including current density, optical bandgap (correlated with open-circuit voltage), and AVT, to give an estimate of the overall LUE figure of merit ( $FoM_{LUE}$ ) for photoactive layer materials.

$$\begin{aligned} \text{FoM}_{\text{LUE}} &= \frac{q}{hc} \int_{300}^{\frac{1240}{Eg}} (1 - T(\lambda)) \times \boldsymbol{\mathcal{D}}_{\text{power}}^{\text{AML.5G}}(\lambda) d(\lambda) \\ &\times \frac{\int_{380}^{740} T(\lambda) \times P(\lambda) \times S(\lambda) d(\lambda)}{\int_{380}^{740} P(\lambda) \times S(\lambda) d(\lambda)} \times \left(\frac{E_g}{q} - 0.3\right) / P_{\text{sun}} \end{aligned} \tag{1}$$

where q is the elementary charge, h is Planck's constant, c is the speed of light, the standardized solar spectral irradiance data ( $\Phi^{\text{AMI.5G}}_{\text{Dower}}(\lambda)$ ) is used from the NREL database,  $T(\lambda)$  is the transmission spectrum,  $E_{\text{g}}$  is the optical bandgap,  $P(\lambda)$  is the photopic response of the human eye,  $S(\lambda)$  is the solar photon flux (AM1.5 G), and  $P_{\text{sun}}$  signifies one sun condition (100 mW cm<sup>-2</sup>). The FoM<sub>LUE</sub> value is expressed as a

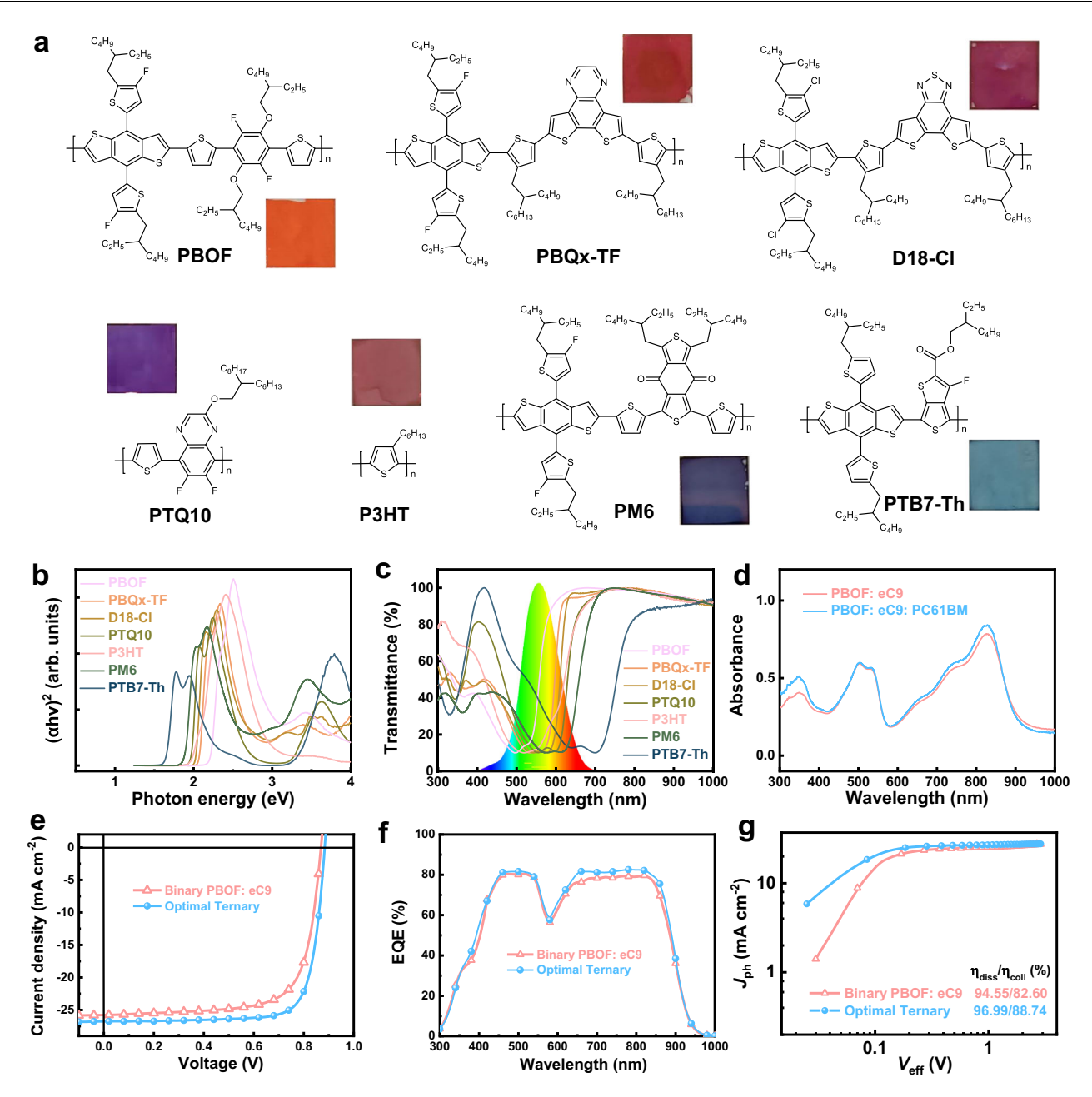


**Fig. 1** | **Characterization of donor and opaque OPV devices. a** The molecular structures and associated thin films (1.5\*1.5 cm²) of representative polymer donors used in this work. **b** The Tauc plot data of donors. **c** The corresponding transmittance spectra of donors. The inserted color map corresponds to the photopic

response of the human eye. **d** The absorption spectra of binary PBOF: eC9 and ternary PBOF: eC9: PC61BM films. **e** J-V curves, **f** EQE spectra, and (**g**) J<sub>ph</sub> versus V<sub>eff</sub> characterization of corresponding binary PBOF: eC9 and optimal ternary PBOF: eC9: PC61BM based opaque devices.

dimensionless parameter. FoM<sub>LUE</sub> is the assessment parameter of photoactive material for ST-OPVs. The distribution of absorption is crucial for the value of FoM<sub>LUE</sub>. A higher FoM<sub>LUE</sub> value of the photoactive layer indicates achievable LUE improvement in the derived ST-OPVs. Herein, the parameter (FoM<sub>LUE</sub>) is used for deducing a material's potential for semitransparent device applications directly from its absorption characteristics, enabling quantitative screening of materials and their combinations. More details are summarized in the Supplementary Note 1.

As this formulation is designed above, we calculate the FoM<sub>LUE</sub> values of state-of-the-art polymer donors, fullerenes, and NFAs. The optical properties of thin films are examined, including transmittance and AVT. As shown in Fig. 1a, the pristine donor films exhibit vivid colors for PBOF, PBQx-TF, D18-Cl, PTQ10, P3HT, PM6, and PTB7-Th.

The optical bandgap values (Tauc plot, Fig. 1b) for these donors are 2.20, 2.07, 2.02, 1.96, 1.95, 1.85, and 1.62 eV, respectively. The normalized absorption (Supplementary Fig. 1) and derived transmittance (Fig. 1c) of these polymer donors are depicted. The FoM<sub>LUE</sub> values of PBOF, PBQx-TF, D18-Cl, PTQ10, P3HT, PM6, and PTB7-Th are calculated as 0.084, 0.050, 0.043, 0.034, 0.042, 0.035, and 0.074, respectively. PBOF exhibits twice the FoM<sub>LUE</sub> value compared to prominent molecules (PM6 and D18-Cl). In the same way, we also investigate the representative acceptors (Supplementary Figs. 2–4). The bandgap and FoM<sub>LUE</sub> values (Supplementary Table 1) are 2.76 eV/0.040, 1.95 eV/0.078, 1.38 eV/0.156, 1.38 eV/0.151, and 1.34 eV/0.161 for PC61BM, PC71BM, L8-BO, eC9-2Cl, and eC9, respectively. The near-infrared NFAs present significantly higher FoM<sub>LUE</sub> values than fullerenes. The FoM<sub>LUE</sub> values of selectively combined donor (PBOF, D18-Cl, PM6, or

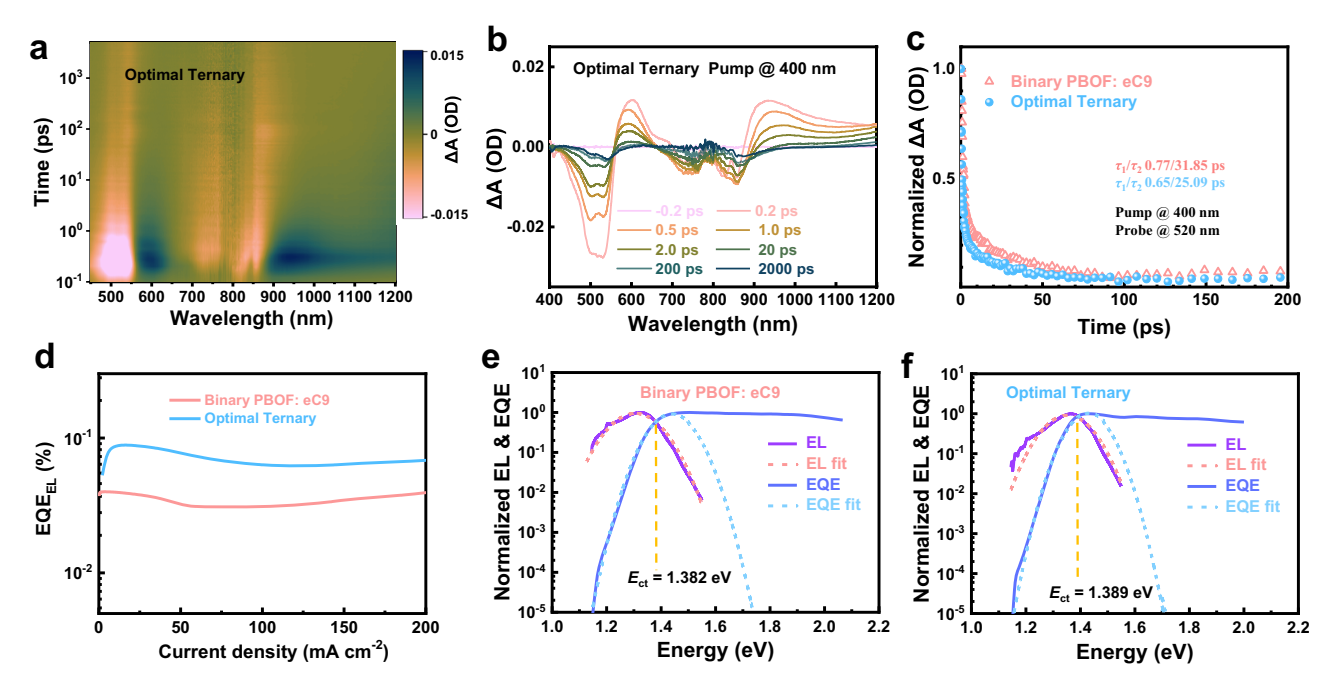


Fig. 2 | Physical properties. a 2D TAS image of optimal ternary blend. b The intensity profiles of the TAS spectra with varied time delays for optimal ternary blend. c The corresponding TAS kinetic lifetimes of binary PBOF: eC9 and optimal

ternary PBOF: eC9: PC61BM blends.  $\mathbf{d}$  EQE<sub>EL</sub> spectra for binary and ternary devices.  $\mathbf{e}$   $E_{\text{CT}}$  determination for binary PBOF: eC9 device.  $\mathbf{f}$   $E_{\text{CT}}$  determination for the optimal ternary device.

PTB7-Th) and acceptor (L8-BO, eC9-2Cl, or eC9) as BHJ layers are also calculated as shown in Supplementary Table 2. The PBOF: eC9 exhibits the highest  $FoM_{LUE}$  value of 0.089. When PC61BM is added as the third component into the PBOF: eC9, the  $FoM_{LUE}$  value of PBOF: eC9: PC61BM can be further increased to 0.091, implying its superior efficiency potential for ST-OPVs.

# **Opaque OPV devices**

We fabricated the opaque OPV devices with an architecture of indium tin oxide (ITO)/HTL/active layer (BHJ)/electron transport layer (ETL)/ silver (Ag) to explore the photovoltaic performance. Hightransparency ITO (Supplementary Fig. 5) is selected with a transmittance (T) of 93.75% at 555 nm and an AVT of 93.16%. Two HTLs, PED-OT:PSS and (4-(7H-dibenzo[c,g]carbazol-7-yl)butyl)phosphonic acid as a self-assembled monolayer (SAM, Supplementary Fig. 6), are compared<sup>40,41</sup>. The AVT of ITO/SAM delivers a higher value of 93.12% than that of ITO/PEDOT:PSS (91.65%), and the ITO/SAM film also exhibits a higher transmittance than the counterpart in the NIR region (740-1000 nm), implying its improved photon harvesting and current density for active layers. The components of PBOF/eC9/PC61BM (binary or ternary, Supplementary Fig. 7) and additives (1,8-diodooctane or 1,3,5-trichlorobenzene<sup>42</sup>) are utilized to optimize the performance of active layers. The absorption spectra of relative films are conducted as shown in Fig. 1d. The binary PBOF: eC9 (Fig. 1e) based devices exhibit a PCE of 16.22% along with  $J_{SC}$  of 25.78 mA cm<sup>-2</sup>,  $V_{OC}$  of 0.869 V, and FF of 72.39%. With 10% wt PC61BM as the third component and 1,3,5-trichlorobenzene as a solid additive, the optimal ternary devices (PBOF: eC9: PC61BM) deliver the highest PCE of 18.60% with enhanced  $J_{SC}$  of 26.75 mA cm<sup>-2</sup>,  $V_{OC}$  of 0.884 V, and FF of 78.66%. Figure 1f depicts the corresponding external quantum efficiency (EQE) characterization. The calculated  $J_{SC}$  values (Supplementary Fig. 8) for binary and optimal ternary devices are 24.59 and 25.54 mA cm<sup>-2</sup>, respectively, within 5% mismatches of the J-V tested ones. The optimal ternary OPV with PEDOT: PSS as HTL produces a lower PCE of 17.58% due to the decreased  $J_{SC}$  of 25.59 mA cm<sup>-2</sup> compared to its counterpart with SAM as HTL (Supplementary Fig. 9). The detailed photovoltaic parameters of various devices, including DIO based one (Supplementary Fig. 10), are summarized in Supplementary Table 3.

#### Physical properties of devices

To investigate the charge recombination processes, the  $I_{SC}$  and  $V_{OC}$  of both binary (PBOF: eC9) and optimal ternary (PBOF: eC9: PC61BM) devices are measured under varying incident light intensities (Plight). The relationship between  $J_{SC}$  and  $P_{light}$  is characterized by the expression  $J \propto P_{\text{light}}^{\alpha}$ . The optimal ternary (PBOF: eC9: PC61BM) device exhibits a higher  $\alpha$  value of 0.982 compared to the binary (PBOF: eC9) device's 0.971 (Supplementary Fig. 11), indicating that bimolecular recombination is suppressed in the optimal ternary (PBOF: eC9: PC61BM) device<sup>43</sup>. Concurrently, the dependence of  $V_{\rm OC}$  and  $P_{\rm light}$  is described by the equation  $V_{OC} \propto \ln(P_{\text{light}}) nkT/q$ , where k represents the Boltzmann constant, T is the Kelvin temperature, and q signifies the elementary charge. Compared to the binary (PBOF: eC9) device's slope of 1.11 kT/q, the optimal ternary (PBOF: eC9: PC61BM) device displays a moderately lower slope of 1.04 kT/q, implying diminished trap-assisted recombination. To quantify exciton dissociation ( $\eta_{\rm diss}$ ) and charge collection ( $\eta_{coll}$ ) efficiencies, an investigation into the photocurrent density  $(I_{ph})$  versus effective voltage  $(V_{eff})$  is conducted by examining the value of  $J_{SC}/J_{sat}$  (the saturation current density) and  $J_{max}/J_{sat}$  in the binary (PBOF: eC9) and optimal ternary (PBOF: eC9: PC61BM) devices<sup>44</sup>. The binary (PBOF: eC9) and optimal ternary (PBOF: eC9: PC61BM) devices (Fig. 1g) yield  $\eta_{\rm diss}/\eta_{\rm coll}$  values of 94.55%/82.60% and 96.99%/88.74%, respectively. The enhancement confirms more effective charge extraction and collection mechanism within the optimal ternary (PBOF: eC9: PC61BM) blend. The charge generation and recombination dynamics are further investigated using femtosecond transient absorption spectroscopy (fs-TAS) upon photoexcitation with a 400 nm laser<sup>45</sup>. Both the PBOF: eC9 (Supplementary Fig. 12) and PBOF: eC9: PC61BM (Fig. 2a) blends exhibit distinct spectral features. A prominent negative-going signals between 470 and 540 nm, consistent with the film's absorption data, originates from the ground-state bleaching (GSB) of PBOF. The kinetics of singlet excited state or localized exciton associated with of PBOF and eC9 produce positive

excited state absorption features around 600 and 950 nm, respectively. To quantify electron transfer kinetics, the decay traces of 520 nm GSB signals in both the PBOF: eC9 (Supplementary Fig. 12) and PBOF: eC9: PC61BM (Fig. 2b) blends are analyzed. A bi-exponential fitting of the decay traces allows for the extraction of lifetime for charge separation  $(\tau_1)$  and charge diffusion  $(\tau_2)$  processes. As shown in Fig. 2c, the PBOF: eC9: PC61BM blend demonstrates shorter lifetimes  $(\tau_1/\tau_2)$  of 0.65/25.09 ps compared to its binary counterpart (0.77/ 31.85 ps). The accelerated processes confirm that the optimal PBOF: eC9: PC61BM ternary blend facilitates more efficient charge separation and diffusion, thereby accounting for its enhanced J<sub>SC</sub> and FF. Furthermore, the hole  $(\mu_h)$  and electron  $(\mu_e)$  mobilities of the PBOF: eC9 and PBOF: eC9: PC61BM blends (Supplementary Fig. 13) are measured with the space-charge-limited-current (SCLC) method, delivering the  $\mu_{\rm b}/\mu_{\rm e}$  values of  $4.37 \times 10^{-4}/2.55 \times 10^{-4}$ ,  $6.52 \times 10^{-4}/5.63 \times 10^{-4} \,{\rm cm}^2{\rm V}^{-1}{\rm s}^{-1}$ , respectively. The higher and more balanced charge mobility ( $\mu_b/\mu_e$  as 1.16) in PBOF: eC9: PC61BM blend is beneficial for suppressing interfacial charge accumulation and promoting more effective charge extraction.

#### Morphological Analysis

The surface and bulk morphologies of the binary (PBOF: eC9) and optimal ternary (PBOF: eC9: PC61BM) blends are characterized through atomic force microscopy (AFM), transmission electron microscopy (TEM), and grazing-incidence wide-angle X-ray scattering (GIWAXS). AFM analysis (Supplementary Fig. 14) indicates that the PBOF: eC9: PC61BM blend has a more uniform surface topography with a root mean square roughness ( $R_{\rm q}$ ) of 2.59 nm than its binary counterpart (3.50 nm). The PBOF: eC9: PC61BM blend forms a more finely dispersed and well-interconnected bicontinuous network (Supplementary Fig. 15), which is beneficial for device performance. We utilize GIWAXS to investigate the molecular ordering and packing behavior within the PBOF: eC9 and PBOF: eC9: PC61BM blends<sup>46</sup>. The PBOF pristine film adopts a mixed face-on and edge-on orientation as depicted in Supplementary Fig. 16. The PBOF: eC9 and PBOF: eC9: PC61BM blend films show distinct packing features as shown in the corresponding line-cut profiles (Supplementary Fig. 17). The PBOF: eC9 blend shows lamellar peaks at  $q_r \approx 0.329 \,\text{Å}^{-1}$  ( $d \approx 19.1 \,\text{Å}$ ) and  $q_z \approx 0.289 \text{ Å}^{-1} (d \approx 21.7 \text{ Å})$ , and  $\pi - \pi$  peak at  $q_z \approx 1.672 \text{ Å}^{-1} (d \approx 3.76 \text{ Å})$ . The PBOF: eC9: PC61BM blend exhibits lamellar peaks at  $q_r \approx 0.305 \,\text{Å}^{-1}$  $(d \approx 20.6 \text{ Å})$  and  $q_z \approx 0.327 \text{ Å}^{-1} (d \approx 19.2 \text{ Å})$ , and  $\pi - \pi$  peak at  $q_z \approx 1.673 \text{ Å}^{-1}$ . The dominant  $\pi$ - $\pi$  stacking peak of the PBOF: eC9: PC61BM blend yields a larger crystalline coherence length (CCL) of 17.8 Å with a full width at half maximum (FWHM) of 0.325 Å<sup>-1</sup>, surpassing the 16.7 Å with a larger FWHM of 0.346 Å<sup>-1</sup> of the PBOF: eC9 blend. The detailed parameters of GIWAXS results are summarized in Supplementary Table 4, signify that the PBOF: eC9: PC61BM blend achieves a more ordered crystalline structure. This improved structural order is directly responsible for facilitating charge transport and suppressing recombination, leading to the higher  $J_{SC}$  and FF in the PBOF: eC9: PC61BM based devices.

# **Energy losses analysis**

We also analyze the energy loss of the binary (PBOF: eC9) and optimal ternary (PBOF: eC9: PC61BM) devices to investigate the origins of the  $V_{\rm OC}$  improvement from 0.869 V to 0.884 V. We first determine the bandgaps ( $E_{\rm g}$ ) to be 1.403 and 1.398 eV for the PBOF: eC9 and PBOF: eC9: PC61BM based devices, respectively (Supplementary Fig. 18). The total energy loss of device ( $E_{\rm loss} = E_{\rm g} \cdot qV_{\rm OC}$ ) is deconstructed into its radiative ( $\Delta E_{\rm 1}$  and  $\Delta E_{\rm 2}$ ) and non-radiative ( $\Delta E_{\rm 3}$ ) recombination loss<sup>47,48</sup>. The fundamental radiative loss ( $\Delta E_{\rm 1}$ ) is nearly identical (-0.262 eV) for the PBOF: eC9 and PBOF: eC9: PC61BM based devices due to similar bandgaps (Supplementary Table 5). The  $\Delta E_{\rm 3}$  is quantified through electroluminescence quantum efficiency (EQE<sub>EL</sub>) measurements (Fig. 2d) using the relation  $\Delta E_{\rm 3} = -\frac{kT}{q}\ln {\rm EQE}_{\rm EL}$ . The PBOF: eC9:

PC61BM based device exhibited a higher EQE<sub>EL</sub> of  $6.21 \times 10^4$ , resulting in a lower  $\Delta E_3$  of 0.191 eV compared to the PBOF: eC9 based device's 0.208 eV. The sub-bandgap radiative loss ( $\Delta E_2$ ) is also modestly reduced from 0.064 eV to 0.061 eV for the PBOF: eC9 and PBOF: eC9: PC61BM based devices. The smaller  $\Delta E_2$  and  $\Delta E_3$  of the optimal ternary (PBOF: eC9: PC61BM) device should be mainly ascribed to the higher energy of the charge transfer state ( $E_{\rm CT}$ ) of 1.389 eV as shown in Fig. 2e, f. Thus, the driving force required for exciton dissociation and non-radiative recombination of optimal ternary (PBOF: eC9: PC61BM) devices is reduced, resulting in decreased energy loss and higher  $V_{\rm OC}$ .

#### Photovoltaic and optical performance of ST-OPVs

For ST-OPVs, the optimal ternary (PBOF: eC9: PC61BM) blends with various thicknesses (50~120 nm) are utilized as the photoactive layers with the thin silver electrode (11 nm) as shown in Supplementary Figs. 19-22. The detailed photovoltaic and optical parameters of derived ST-OPVs are summarized in Supplementary Table 6. With the decreasing thickness from 120 nm to 50 nm (Fig. 3a), the J<sub>SC</sub> and PCE values of ST-OPVs are sequentially decreased from 22.25 mA cm<sup>-2</sup>/ 15.23% to 16.37 mA cm<sup>-2</sup>/10.74%, respectively, while the AVT values are gradually increased from 23.23% to 37.57% as shown in Fig. 3b. The 60-nm ST-OPVs achieve the highest LUE of 4.12% along with a PCE of 11.81% and an AVT of 34.80%. To further improve the LUE value of ST-OPVs, two optical designs are employed atop the thin silver electrode: a single-layer antireflection coating layer using TeO2 as the optical interference materials<sup>49</sup> and an aperiodic band-pass filter<sup>22</sup> (ABPF, Supplementary Table 7) with total reflection in the NIR region (700-900 nm). As shown in Fig. 3c, compared to the bare 11-nm Ag based ST-OPVs (AVT of 34.80%), both the ST-OPVs with 40-nm TeO<sub>2</sub> or ABPF exhibit significantly improved transparency in the visible region, resulting in increased AVT of 50.86% and 49.62%, respectively. It is worth noting that the single-layer antireflection coating layer (40-nm TeO<sub>2</sub>) increases the transmittance of the device in the whole range from 350 nm to 1,000 nm, resulting in a noticeable decrease in J<sub>SC</sub>. ST-OPVs with ABPF almost completely block light in the range of 700-900 nm, which makes a decent contribution to the ST-OPV's J<sub>SC</sub>. The J-V curves of corresponding 11-nm Ag, 40-nm TeO<sub>2</sub>, and ABPF based ST-OPVs are depicted in Fig. 3d. The  $V_{\rm OC}$  and FF values among the devices are similar. Compared to 11-nm Ag based ST-OPV (17.35 mA cm<sup>-2</sup>), the  $J_{SC}$  of ST-OPV with 40-nm TeO<sub>2</sub> decreased to 15.63 mA cm<sup>-2</sup> while that of ST-OPV with ABPF increased to 18.07 mA cm<sup>-2</sup>, impacting their efficiencies. The 11-nm Ag, 40-nm TeO<sub>2</sub>, and ABPF-based ST-OPVs (Fig. 3e and Table 1) achieve PCEs of 11.84%, 10.47%, and 12.19%, delivering LUEs of 4.12%, 5.32%, and 6.05%, respectively. The LUE of 6.05% as the figure of merit for all semitransparent solar cells is the highest value in the literature (Fig. 3f and Supplementary Table 8). The influence of optical layers on  $J_{SC}$  is also investigated using the external quantum efficiency (EQE) characterization (Supplementary Fig. 23). The J<sub>SC</sub> values calculated for 11-nm Ag, 40-nm TeO2, and ABPF-based ST-OPVs are 16.62, 14.89, and 17.18 mA cm<sup>-2</sup>, respectively. Compared to 11-nm Ag based ST-OPV, the 40-nm TeO2 based device exhibits a weaker photon response in the whole range, which correlates to the lower J<sub>SC</sub>. The ABPF-based ST-OPV demonstrates similar weaker photon responses in the 300-400 nm range, but substantially stronger photon responses in the 700-900 nm range.

The optical analysis of corresponding ST-OPVs, including reflectance, quantum utilization efficiency (QUE = EQE + T), and EQE + T + R, are also measured to validate the accuracy and validity of J-V measurements as shown in Supplementary Fig. 24<sup>50</sup>. All the EQE( $\lambda$ ) +  $T(\lambda)$  +  $R(\lambda)$  values are below 100%. It is noticed that the quantum utilization efficiency of ABPF-based ST-OPV exhibits a lower value in the range of 700–900 nm compared to others, due to its combined effect of inherently strong reflection of ABPF and thin active layer's weak absorption. To further verify the difference and variation trend of

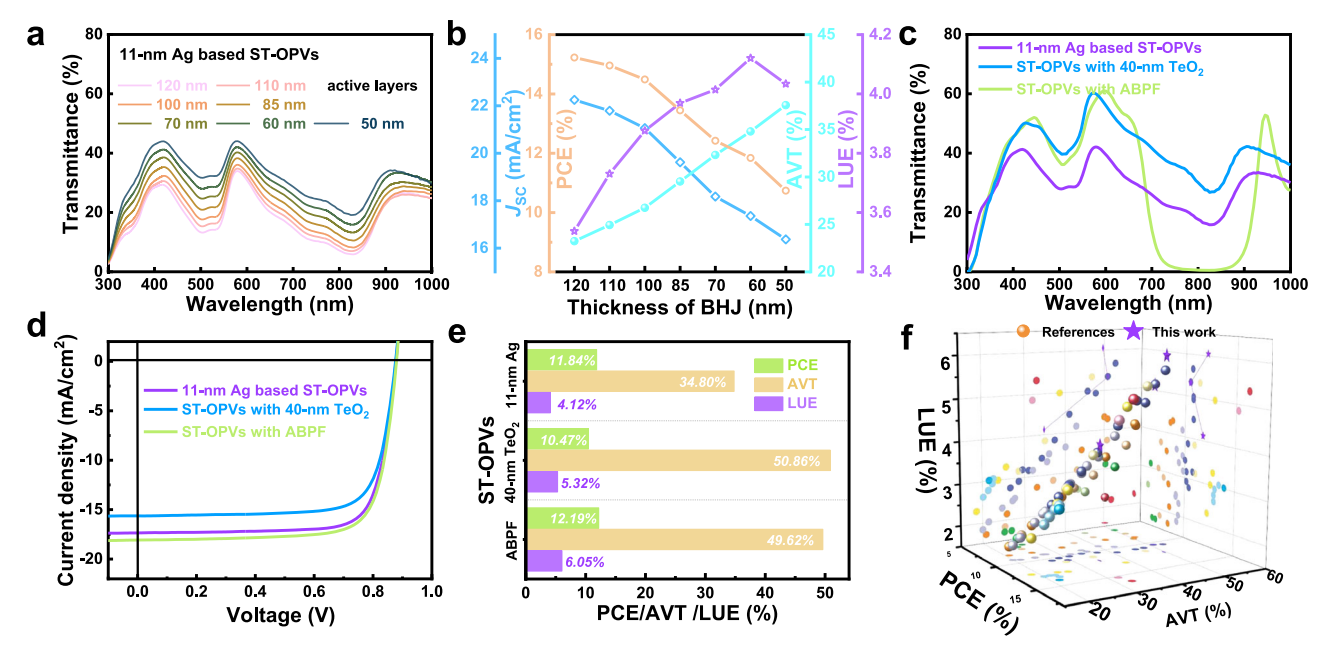


**Fig. 3** | **Characterization of ST-OPVs. a** The transmittance spectra of 11-nm Ag based ST-OPVs with various active layers thicknesses. **b** The  $J_{SC_i}$  PCE, AVT, and LUE of the ST-OPVs with various active layer thicknesses. **c** The transmittance spectra of

11-nm Ag, 40-nm  $TeO_2$ , and ABPF based ST-OPVs.  $\mathbf{d}$  The J-V curves of corresponding ST-OPVs.  $\mathbf{e}$  The PCE, AVT, and LUE of corresponding ST-OPVs.  $\mathbf{f}$  Comparison of LUE versus PCE and AVT values in reported semitransparent solar cells.

Table 1 | The photovoltaic and optical parameters of selected opaque and semitransparent devices based on optimal ternary active layers

Devices	V <sub>oc</sub> (V)	J <sub>SC</sub> (mA cm <sup>-2</sup> )	Cal. J <sub>SC</sub> (mA cm <sup>-2</sup> )	FF (%)	PCE <sup>a</sup> (%)	AVT (%)	LUE (%)
opaque	0.884	26.75	25.54	78.66	18.60 (18.43 ± 0.13)	-	-
11-nm Ag	0.878	17.35	16.62	77.69	11.84 (11.61 ± 0.15)	34.80	4.12
40-nm TeO <sub>2</sub>	0.877	15.63	14.89	76.37	10.47 (10.21 ± 0.14)	50.86	5.32
ABPF	0.880	18.07	17.18	76.63	12.19 (11.83 ± 0.17)	49.62	6.05

<sup>&</sup>lt;sup>a</sup>The average PCE values with standard deviation are obtained from over 10 devices.

corresponding 11-nm Ag, 40-nm TeO<sub>2</sub>, and ABPF based ST-OPVs, the optical simulations of current density and optoelectronic field intensity distribution in devices are carried out. The refractive indices of materials used in this work are listed in Supplementary Fig. 25. The simulated transmittance spectra (Fig. 4a) and J<sub>SC</sub> values (Fig. 4b) of 11-nm Ag, 40-nm TeO<sub>2</sub>, and ABPF-based ST-OPVs show the same trend compared with the experimental ones (Supplementary Fig. 26). The difference in simulated  $J_{SC}$  using 11-nm Ag device as the baseline is depicted in Fig. 4c, resulting in a decreased  $J_{SC}$  of 3.98 mA cm<sup>-2</sup> and an increased  $J_{SC}$ of 1.40 mA cm<sup>-2</sup> for 40-nm TeO<sub>2</sub>, and ABPF-based ST-OPVs, respectively. The optical field  $|\mathbf{E}|^2$  distribution (Supplementary Fig. 27) and corresponding exciton generation rates (Fig. 4d-f) of relative ST-OPVs (60-nm active layer) are carried out. The 40-nm TeO<sub>2</sub>-based ST-OPV exhibits lower simulated exciton generation rates in the whole region than its counterpart with barely 11-nm Ag one. The ABPF-based ST-OPV presents significantly higher exciton generation rates in the 700-900 nm range. The difference in the exciton generation rate of ST-OPVs with 11-nm Ag as a baseline is calculated as shown in Supplementary Fig. 28. The results indicate the effective optical management of 40-nm TeO<sub>2</sub> and ABPF structures in devices. The operational stability (light-socking, ISOS-L-1, Supplementary Fig. 29) of these ST-OPVs is conducted under a continuous light-emitting diode light, which is equivalent to AM1.5 G illumination<sup>51,52</sup>. More detailed device stability measurements are summarized in the "Methods" section. The  $T_{80}$ lifetime (80% of the initial PCE, Fig. 4g) of encapsulated 11-nm Ag, 40-nm TeO<sub>2</sub>, and ABPF-based ST-OPVs are 250 h, 562 h, and 835 h, respectively. The results indicate the effective protection of the optical

layer (TeO $_2$  or ABPF) as a buffer layer in the encapsulation for ST-OPVs $^{22,24}$ .

#### Aesthetic and functional transparency of ST-OPVs

In the applications of ST-OPVs like smart windows and buildingintegrated photovoltaics (BIPV), color rendering index (CRI) plays a pivotal role in balancing energy harvesting with aesthetic and functional transparency, which is a critical parameter in assessing the quality of light as perceived by the human eye when a natural or standard light source transmitted through the device. CRI value is expressed on a scale from 0 to 100. Achieving a higher CRI (over 80) ensures that ST-OPVs can seamlessly integrate into environments requiring accurate color perception. Herein, the CRI value of 11-nm Ag based ST-OPVs gradually increases from 87.1 to 95.1 as the thickness of active layers decreases from 120 nm to 50 nm. When the active layer's thickness is 60 nm, the corresponding 11-nm Ag, 40-nm TeO<sub>2</sub>, and ABPF based ST-OPVs (Supplementary Table 9) exhibit CRI values of 94.4, 93.9, and 90.5, respectively. The correlated color temperature (CCT) values of corresponding 11-nm Ag, 40-nm TeO<sub>2</sub>, and ABPF based ST-OPVs are 4966 K, 4800 K, and 4465 K, respectively, where the AM1.5 G possesses a CCT of 5513 K. The medium CCT between 4000 K and 5000 K means a neutral white color appearance. The CIE 1931 chromaticity diagram provides a method to quantify color perception using two-dimensional coordinates (x, y). We evaluate the color properties of these ST-OPVs by comparing their coordinates to the standard daylight illuminant AM1.5 G (0.332, 0.343). The CIE color coordinates of corresponding 11-nm Ag, 40-nm TeO<sub>2</sub>, and ABPF based

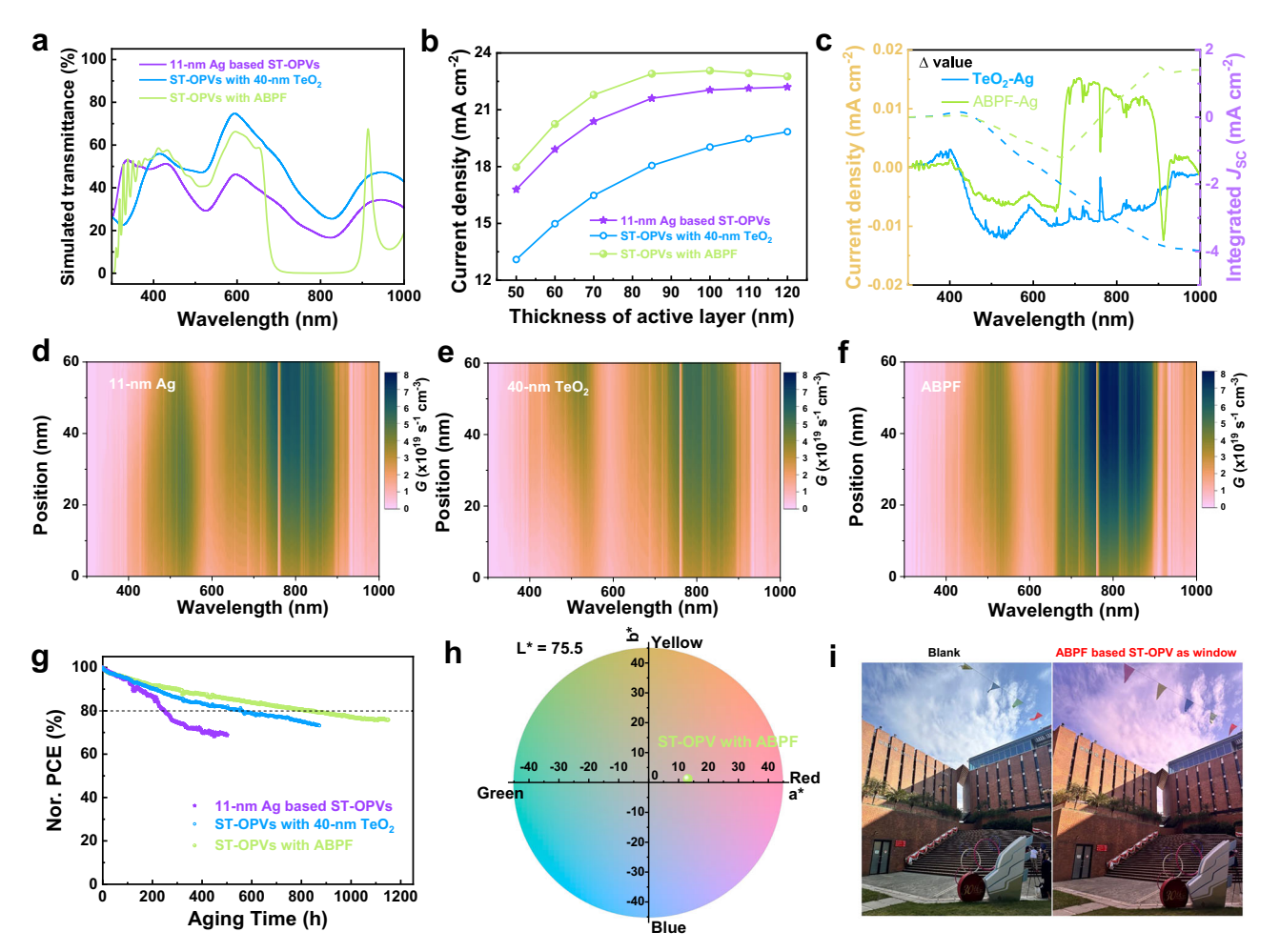


**Fig. 4** | **Optical simulation and functional transparency of ST-OPVs. a** The calculated transmittance spectra of 11-nm Ag based ST-OPVs with various active layers thicknesses. **b** The calculated  $J_{SC}$  of ST-OPVs with various active layer thicknesses. **c** The difference in the calculated  $J_{SC}$  of ST-OPVs with 11-nm Ag one as the baseline. The exciton generation rates (*G*) of (**d**) 11-nm Ag, (**e**) 40-nm TeO<sub>2</sub>, and (**f**) ABPF

based ST-OPVs. **g** The operational stability (light-socking, ISOS-L-1) of corresponding ST-OPVs. **h** CIELAB coordinate space of ST-OPV with ABPF. **i** Photograph of blank and ABPF based ST-OPV as window. The background features The Hong Kong Polytechnic University building to illustrate device transparency.

ST-OPVs are (0.345, 0.334), (0.350, 0.345), and (0.357, 0.335), respectively. As illustrated in Supplementary Fig. 30, these coordinates closely approach the AM1.5 G coordinates, presenting a reddish hue. The CIELAB coordinates ( $L^*$ ,  $a^*$ ,  $b^*$ ) of these devices (Supplementary Note 2) are also employed to more intuitively compare their differences of aesthetic transparency, where L\* coordinate quantifies lightness from 0 (black) to 100 (diffuse white), a\* coordinate spans the green-red spectrum (negative for green, positive for red), and  $b^*$ coordinate spans the blue-yellow spectrum (negative for blue, positive for yellow). As shown in Supplementary Fig. 31 and Fig. 4h, the CIELAB coordinates  $(L^*, a^*, b^*)$  of corresponding 11-nm Ag, 40-nm TeO<sub>2</sub>, and ABPF based ST-OPVs are (65.4, 7.78, -0.99), (76.4, 6.43, 3.38), and (75.5, 13.2, 1.36), respectively, indicating the aesthetic transparency of these devices. To illustrate the visibility and color of these ST-OPVs, we photograph The Hong Kong Polytechnic University building and color A4 paper as backgrounds, viewed through transparent device as a window. These photographs present a reddish hue as shown in Fig. 4i and Supplementary Fig. 32.

#### Thermal insulation performance of ST-OPVs

The thermal insulation performance of these ST-OPVs (Supplementary Note 3) is quantified through the measured NIR (NIR-SER, 780–2500 nm) and total solar energy rejection (T-SER, 300–2500 nm). The NIR-SER and T-SER values (Supplementary Fig. 33) of

corresponding 11-nm Ag, 40-nm TeO<sub>2</sub>, and ABPF based ST-OPVs are 82.91%/75.79%, 78.82%/67.67%, and 88.43%/77.49%, respectively. The results indicate the superior thermal insulation capabilities of these devices, especially the ABPF based ST-OPV. Their thermal insulation performance is intuitively explored by putting up a prefabricated structure as shown in Supplementary Fig. 34. A black object in the foam box can be illuminated through different windows, and the temperature changes of the black object are recorded by a Fluke infrared thermal imaging camera. As shown in Supplementary Fig. 35 (visible mode by the camera) and Fig. 5a (IR mode), the object at 24.2 °C is recorded before illumination. After 10-min solar simulator illumination, the temperature of the object reaches 50.0, 45.1, 37.4, 37.6, and 36.4 °C through air, glass, 11-nm Ag, 40-nm TeO<sub>2</sub>, and ABPF based ST-OPVs as the windows, respectively (Fig. 5). Considering the power generation and thermal insulation capabilities, the ABPF based ST-OPVs exhibit the best multifunctional performance, revealing its promise potential in the field of BIPVs as smart windows.

#### ST-OPVs as smart windows

To explore the power generation and energy-saving performance of the ST-OPV glazing window, we develop a transient model to simulate the power output and assess the impact on building space cooling and heating loads. As shown in Fig. 6a, a typically used double-glazed window structure is designed, with the configuration of ST-OPV/air gap

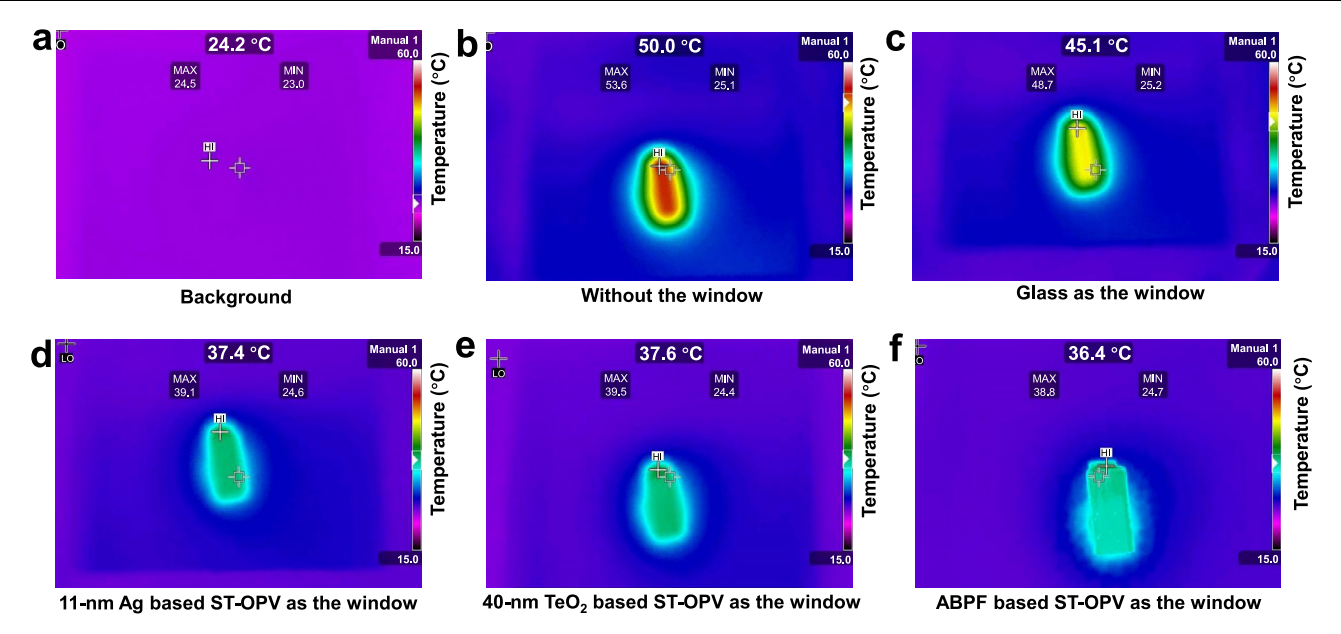


**Fig. 5** | **Thermal insulation performance of ST-OPVs as windows.** The temperature (°C) changes are recorded by a Fluke infrared thermal imaging camera under the IR mode. The colored scale bars represent temperature from 15 to 60 °C. **a** The

temperature of the object before illumination. The temperature of the object after 10-min solar simulator illumination with different windows,  $(\mathbf{b})$  without,  $(\mathbf{c})$  glass,  $(\mathbf{d})$  11-nm Ag,  $(\mathbf{e})$  40-nm TeO<sub>2</sub>, and  $(\mathbf{f})$  ABPF based ST-OPVs.

(12 mm)/glazing. A double-layered low-e window is used as the base-line for comparison in the simulation, due to its versatility in meeting diverse environmental requirements, such as providing thermal insulation and soundproofing benefits. The spectral transmittance and reflectance of low-e glazing are given in Supplementary Fig. 36. The simulations are conducted among 371 cities across China (Ministry of Natural Resources of the People's Republic of China, GS (2019)1822), which are located in five different climatic zones classified by "Code for Thermal Design of Civil Buildings", namely, severe cold, cold, hot summer/cold winter, mild, and hot summer/warm winter zones respectively (Supplementary Fig. 37)<sup>53</sup>. A detailed description of the simulation conditions, including hourly meteorological data, geographical factors (latitude and altitude, Supplementary Fig. 38), and spectral power distribution (SPD) of solar radiation (Supplementary Fig. 39) is provided in the Supplementary Note 4.

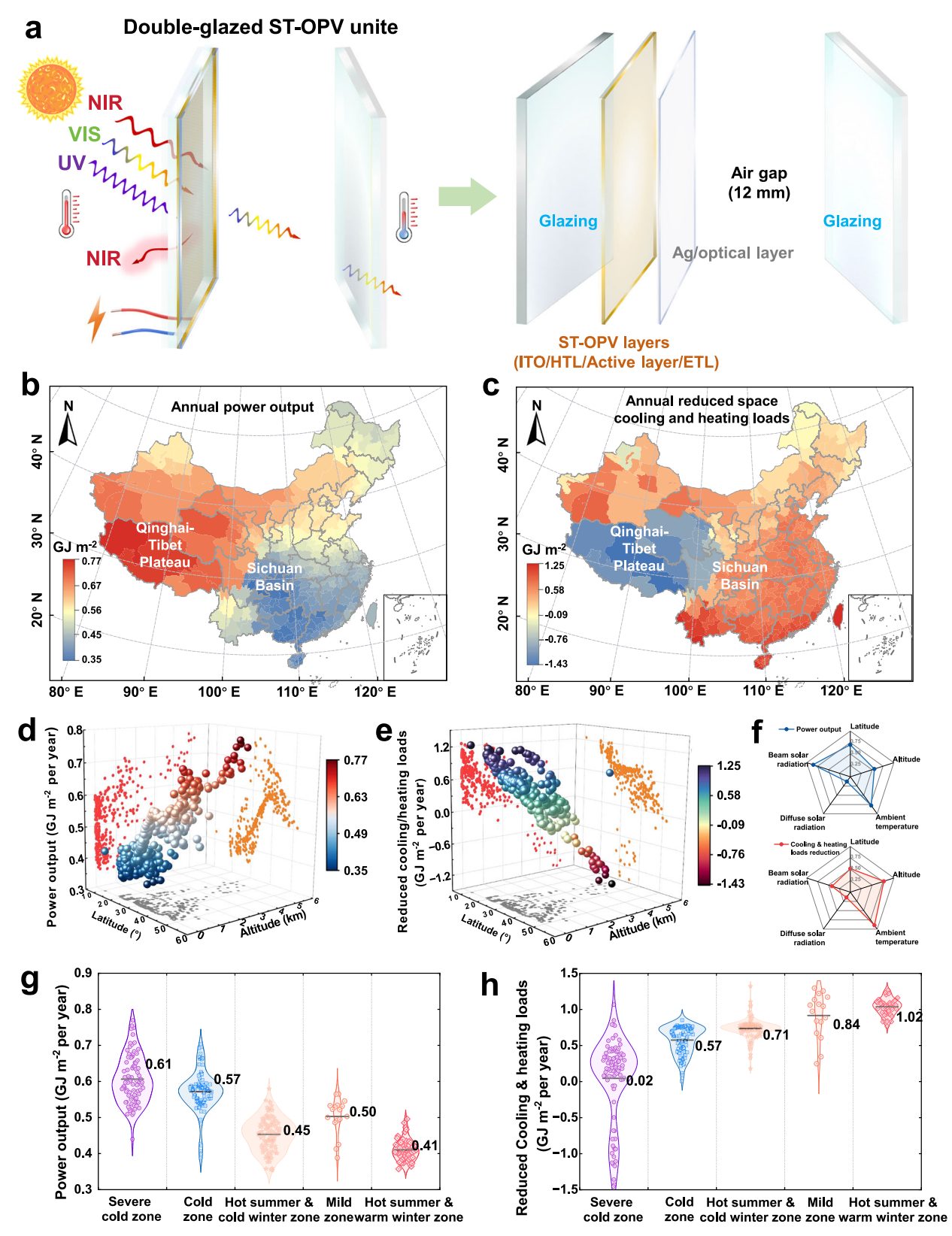
As shown in Fig. 6b, the window with ABPF-based ST-OPV annually generates 0.35 to 0.77 GJ m<sup>-2</sup> electrical power in different climatic zones. From another perspective, the solar absorbing properties of ST-OPV windows will help reduce building space cooling loads during the hot seasons, while negatively increasing building space heating loads in cold climates. The annually reduced space cooling load and increased space heating load for the ABPF-based ST-OPV window among the 371 cities are depicted in Supplementary Fig. 40. Figure 6c visualizes the annual load reduction (which equals the reduced cooling load minus the increased heating load), which ranges from -1.43 to 1.25 GJ m<sup>-2</sup> across different regions in China. For most regions (348 out of 371 cities), the annual load reductions are positive, except for regions with high heating demands (Supplementary Fig. 41). The negative values are mainly observed in western China, for example Qinghai-Tibet Plateau. This is primarily attributed to the unique geographical conditions of high altitude, which lead to high building space heating loads throughout the year.

Figure 6d and Fig. 6e clarify the effects of geographical factors on annual power output and annual load reduction of the ABPF-based ST-OPV window, respectively. The annual power output exhibits an increasing trend as latitude rises from  $20^\circ$  to  $40^\circ$ , whereas it decreases when moving from  $40^\circ$  to  $50^\circ$ . To further evaluate the correlation among complex variables (beam solar radiation, diffuse solar

radiation, latitude, altitude, and ambient temperature) on annual power output and load reduction, the Pearson correlation coefficients are calculated, as shown in Fig. 6f. The results indicate that the annual power output is most sensitive to the level of beam solar radiation, while the annual load reduction is primarily influenced by the ambient temperature and altitude, as evidenced by Pearson correlation coefficients exceeding 0.5. As shown in Fig. 6g, the statistical results demonstrate that the average annual power output values of the ABPFbased ST-OPV windows are 0.61, 0.57, 0.45, 0.50, and 0.41 GJ m<sup>-2</sup> for severe cold, cold, hot summer/cold winter, mild, and hot summer/ warm winter zones, respectively. Correspondingly, the average load reductions (Fig. 6h) are 0.02, 0.57, 0.71, 0.84, and 1.02 GJ m<sup>-2</sup>, respectively. Among the five climatic zones, the hot summer/warm winter zone exhibits the highest energy-related performance of the ABPF-based ST-OPV window, with total power output and load reduction of 1.43 GJ m<sup>-2</sup> (Supplementary Table 10). Similar results are also observed for the double-glazed window with 11-nm Ag or 40-nm TeO<sub>2</sub> based ST-OPVs glazing, as shown in Supplementary Figs. 42–47. Considering the total power generation and load reduction of the ST-OPV window, the hot summer/warm winter zone is the most suitable for ST-OPVs as a window, as it achieves the optimal balance between power generation and energy-saving.

#### **Discussion**

In conclusion, a dimensionless parameter ( $FoM_{LUE}$ ) has been established to evaluate the potential of photoactive materials for ST-OPVs, taking into account three aspects: AVT, bandgap, and current density, through investigating the normalized absorbance of photoactive materials. PBOF and eC9 exhibit the highest  $FoM_{LUE}$  values of 0.084 and 0.161 for the investigated donors and acceptors, respectively. The PBOF: eC9 active layer exhibited the highest  $FoM_{LUE}$  value of 0.089 in the binary blends. When PC61BM is added as the third component into the PBOF: eC9, the  $FoM_{LUE}$  value of PBOF: eC9: PC61BM can be further increased to 0.091. The photovoltaic performance of ITO/SAM/PBOF: eC9: PC61BM /PFN-Br/Ag based devices delivers the highest PCE of 18.60%. Compared to its counterpart, the optimal PBOF: eC9: PC61BM ternary blend exhibits higher and more balanced charge mobility, and a more ordered crystalline structure with well-defined molecular



**Fig. 6** | **Simulation of ST-OPVs as smart windows. a** The schematic diagram of the used double-glazed window structure. **b** The annual power out and (**c**) annual load reduction diagram of the window with ABPF-based ST-OPV across China (Ministry of Natural Resources of the People's Republic of China, GS (2019)1822). The effects

of geographical factors on  $(\mathbf{d})$  annual power output and  $(\mathbf{e})$  annual load reduction of the ABPF-based ST-OPV window.  $\mathbf{f}$  Pearson correlation coefficients. The statistical results of average annual  $(\mathbf{g})$  power output and  $(\mathbf{h})$  load reduction values in five different climatic zones.

packing, leading to reduced charge recombination losses and more effective charge transport and extraction. The decreased energy loss and higher  $V_{\rm OC}$  are attributed to the reduced driving force of optimal ternary (PBOF: eC9: PC61BM) devices. For ST-OPVs, the 11-nm Ag, 40nm TeO2, and ABPF-based ST-OPVs achieve PCEs of 11.84%, 10.47%, and 12.19%, and AVT of 34.80%, 50.86%, and 49.62%, delivering LUEs of 4.12%, 5.32%, and 6.05%, respectively. The LUE of 6.05% as the figure of merit for semitransparent solar cells is the highest value. The optical analyses of corresponding ST-OPVs, including optical simulation and EQE + T + R, are utilized to validate the trend and validity of our results. The higher  $T_{80}$  lifetime of encapsulated ABPF-based ST-OPVs is 835 h due to the effective protection of the optical layer as a buffer layer. The aesthetic transparency of these devices presents a reddish hue. These ST-OPVs exhibited superior thermal insulation performance with the NIR-SER and T-SER of 82.91%/75.79%, 78.82%/67.67%, and 88.43%/ 77.49%, respectively. The thermal insulation capabilities of these devices as a window are also qualified by setting up a prefabricated structure where a black object in the foam box can be illuminated through different windows. The qualified thermal insulation results demonstrate the superior multifunctional performance of the ABPF based ST-OPVs as smart windows. The derived ST-OPV glazing window provides positive annual load reductions for over 90% of cities (348 out of 371) in China. Considering the total power generation and energy-saving performance of a double-glazed window with ST-OPV across China with five different climatic zones, the hot summer/warm winter zone is the most suitable for ST-OPVs as a window, delivering an average annual energy-saving of 1.43 GJ m<sup>-2</sup>. Our results highlight the multifunctionality and the influence of geographical factors on the record-efficiency ST-OPVs, demonstrating their potential in aesthetically and functionally demanding applications.

#### Methods

#### **Materials**

The polymer donors and non-fullerene acceptors (PM6, D18-Cl, PBQx-TF, eC9, eC9-2Cl and L8-BO) are procured from Solarmer Materials Inc. Other polymers, including P3HT, PTQ10 and PTB7-Th are obtained from Rieke Metals and 1-Material Inc., respectively. The polymer PBOF is synthesized via Stille cross-coupling polymerization. The reaction involves the copolymerization of two monomers, including the stannylated monomer (4,8-Bi(5-(2-ethylhexyl)-4-fluorothiophen-2-yl) benzo[1,2-b:4,5-b']dithiophene-2,6-diyl)bis(trimethylstannane) and the brominated monomer 5,5'-(2,5-Bis((2-ethylhexyl)oxy)-3,6-difluoro-1,4phenylene)bis(2-bromothiophene). The fullerene derivatives (PC61BM and PC71BM) are sourced from American Dye Source Inc. The PEDOT: PSS (CLEVIOS™ P VP AI 4083, Heraeus) and the SAM interface layer (TCI) are also commercially sourced. All other reagents and solvents are purchased from Sigma-Aldrich and used as received.

#### **Device fabrications**

High-transparency ITO-coated glass substrates (15 Ω sq<sup>-1</sup>) are cleaned via sequential ultrasonication in detergent, deionized water, acetone, and isopropanol. Prior to deposition, all substrates are treated with UV ozone for 15 min. Two different HTLs are used. For the SAM, a 0.5 mg mL<sup>-1</sup> solution in isopropanol is spin-coated at 4000 rpm and annealed (100 °C, 10 min). PEDOT: PSS layer is spin-coated at 5000 rpm and annealed (150 °C, 15 min). The active layer solutions, consisting of either binary PBOF: eC9 (1:1.5) or ternary PBOF: eC9: PC61BM (1:1.5:0.1) in chlorobenzene (8–10 mg ml<sup>-1</sup>) with DIO (0.25% v/v) or TCB (10 mg mL<sup>-1</sup>) as additives, are stirred at 60 °C. In a nitrogen-filled glovebox, the solutions are spin-coated (2500–5500 rpm) atop the HTL and subsequently annealed at 100 °C for 5 min. Film thickness is measured with a Bruker DektakXT Surface Profiler. A cathode layer of PFN-Br/PDINN (0.5/1 mg ml<sup>-1</sup>) is spin-coated at 3000 rpm for 30 s. The devices are completed by thermally evaporating Ag rear electrodes (either 100 nm or 11 nm thick) through a mask at a rate of 1.0 Å s<sup>-1</sup> under

high vacuum ( $10^4$ Torr), defining an active area of 0.042 cm<sup>2</sup>. Additional layers such as TeO<sub>2</sub> and ABPF are deposited at 1.0-2.0 Å s<sup>-1</sup> for LiF and TeO<sub>2</sub>.

#### **Device characterizations**

The *J-V* characteristics of the photovoltaic devices are determined using a Keithley 2400 source measurement unit under simulated AMI.5 G illumination from a Class AAA solar simulator (Enli Technology, SS-F7). The light intensity is calibrated to 100 mW cm<sup>-2</sup> using a KG-5 filtered silicon reference cell. To ensure accuracy of photovoltaic efficiency, a metal mask aperture (0.0324 cm<sup>2</sup>) is used to define the active area for *J-V* test. The *J-V* curves are recorded by sweeping from short-circuit to open-circuit with a 0.02 V step size and no delay time. No light soaking or external bias is applied to the devices before measurement. EQE and reflection spectra are measured using a Solar Cell Spectral Response Measurement System (Enli Technology, QE-R3011). The absorption and transmission spectra of the films are recorded from 300 to 1100 nm using a UV-vis spectrometer (Persee, TU-1810).

#### The calculation formula for thermal insulation

The concepts of T-SER and NIR-SER provide a quantitative framework for assessing the energy-saving performance of common tinted window films.

$$T - SER = \frac{\int_{300}^{2500} [1 - T(\lambda)] P_{AMI.5G}(\lambda) d\lambda}{\int_{300}^{2500} P_{AMI.5G}(\lambda) d\lambda} = \frac{\int_{300}^{2500} [R(\lambda) + A(\lambda)] P_{AMI.5G}(\lambda) d\lambda}{\int_{300}^{2500} P_{AMI.5G}(\lambda) d\lambda}$$
(2)

$$NIR - SER = \frac{\int_{780}^{2500} [R(\lambda) + A(\lambda)] P_{AML.5G}(\lambda) d\lambda}{\int_{780}^{2500} P_{AML.5G}(\lambda) d\lambda}$$
(3)

where  $T(\lambda)$ ,  $R(\lambda)$ , and  $A(\lambda)$  denote the wavelength dependent transmittance, reflectance, absorbance of the device, measured from 300–2500 nm with a HITACHI UH4150 spectrometer. The  $P_{\text{AMI.5G}}(\lambda)$  signifies the standard AM1.5 G photon flux solar power density spectrum (ASTM GI73-03).

#### **Devices stability measurement**

The operational stability of the devices is assessed according to the ISOS-L-1 protocol, which involves continuous maximum power point tracking (MPPT). For the measurement, each device is encapsulated inside a nitrogen glovebox by sealing it with a glass coverslip and UV-curable epoxy. The encapsulated device is maintained at a constant temperature of ~25 °C using a continuous cooling fan. The illumination is provided by a LED lamp with an intensity of 100 mW cm². The spectrum of the LED source is characterized using a calibrated Ocean Optics spectral radiometer.

# **Optical simulation**

We employ the transfer matrix method (TMM) for optical modeling to calculate the device properties, including the transmittance  $(T(\lambda))$ , optical electric field intensity distribution ( $|\mathbf{E}(x, \lambda)|^2$ ), and exciton generation profile (G(x)). The model assumes perfectly planar interfaces and optically isotropic layers. The complex refractive index (n+ik) for each materials are determined experimentally using variable angle spectroscopic ellipsometry (J. A. Woollam, WVASE32). The position-dependent exciton generation rate (G(x)) within the active layer is determined from the calculated optical electric field intensity and the material's absorption coefficient ( $\alpha = 4\pi k/\lambda$ ). The theoretical maximum short-circuit current density ( $J_{SC}$ ) is subsequently calculated by integrating G(x) over the active layer thickness, assuming 100% IQE and using the standard AM1.5 intensity spectrum (ASTM G173-03).

#### Characterizations

An integrated system (Enlitech, PECT-600) is employed for highly sensitive EOE measurements. Electroluminescence EOE characterization is conducted with an ELCT-3010 system (Enlitech). Surface topograpgy is analyzed using a Bruker nanoscope 8 for AFM measurements and a tungsten thermionic emission SEM system (IEOL Model JSM-6490) for SEM measurements. The grazing incident wideangle X-ray scattering (GIWAXS) is performed at the 1W1A-Diffuse Scattering Experiment station of the Beijing Synchrotron Radiation Facility (BSRF). These measurements use an X-ray source of 1.546 Å with an incidence angle of 0.3°. The samples for GIWAXS measurements are prepared on silicon substrates. The photophysical dynamics are explored via femtosecond transient absorption (fs-TA) spectroscopy, conducted with an ultrafast pump/probe detection systems (HELIOS). Thin film samples are prepared by spin-coating the active layer atop quartz substrates. The excitation power is maintained below 20 nJ per pulse to mitigate the effects of exciton-exciton annihilation. The charge transport properties (SCLC mobility) are evaluated by fabricating hole/electron only devices. SCLC mobility are extracted by fitting the dark current to the Mott-Gurney law.

## Reporting summary

Further information on research design is available in the Nature Portfolio Reporting Summary linked to this article.

#### Data availability

All data supporting the findings of this study are available within the main text and Supplementary Information file. Additional data are available from the corresponding author on request. Source data are provided with this paper.

#### References

- Ballif, C., Perret-Aebi, L.-E., Lufkin, S. & Rey, E. Integrated thinking for photovoltaics in buildings. *Nat. Energy* 3, 438–442 (2018).
- Li, Y., Huang, X., Sheriff, H. K. M. & Forrest, S. R. Semitransparent organic photovoltaics for building-integrated photovoltaic applications. *Nat. Rev. Mater.* 8, 186–201 (2023).
- Traverse, C. J., Pandey, R., Barr, M. C. & Lunt, R. R. Emergence of highly transparent photovoltaics for distributed applications. *Nat. Energy* 2, 849–860 (2017).
- Prince, K. J. et al. Holistic thermo-optical design of laminate layers for halide perovskite photovoltaic windows. ACS Energy Lett 9, 5836–5849 (2024).
- Hou, J., Inganäs, O., Friend, R. H. & Gao, F. Organic solar cells based on non-fullerene acceptors. *Nat. Mater.* 17, 119–128 (2018).
- Cheng, P., Li, G., Zhan, X. & Yang, Y. Next-generation organic photovoltaics based on non-fullerene acceptors. *Nat. Photon.* 12, 131–142 (2018).
- Yan, C. et al. Non-fullerene acceptors for organic solar cells. Nat. Rev. Mater. 3, 18003 (2018).
- Liu, F. et al. Efficient semitransparent solar cells with high NIR responsiveness enabled by a small-bandgap electron acceptor. Adv. Mater. 29, 1606574 (2017).
- 9. Yu, H. et al. Semi-transparent organic photovoltaics. *Chem. Soc. Rev.* **52**, 4132–4148 (2023).
- Zhu, L. et al. Achieving 20.8% organic solar cells via additiveassisted layer-by-layer fabrication with bulk p-i-n structure and improved optical management. *Joule* 8, 3153–3168 (2024).
- Fu, J. et al. Rational molecular and device design enables organic solar cells approaching 20% efficiency. *Nat. Commun.* 15, 1830 (2024).
- Sun, Y. et al. π-extended nonfullerene acceptor for compressed molecular packing in organic solar cells to achieve over 20% efficiency. J. Am. Chem. Soc. 146, 12011–12019 (2024).

- 13. Jiang, Y. et al. Non-fullerene acceptor with asymmetric structure and phenyl-substituted alkyl side chain for 20.2% efficiency organic solar cells. *Nat. Energy* **9**, 975–986 (2024).
- Zhang, M., Guo, X., Ma, W., Ade, H. & Hou, J. A large-bandgap conjugated polymer for versatile photovoltaic applications with high performance. Adv. Mater. 27, 4655–4660 (2015).
- Sun, C. et al. A low cost and high performance polymer donor material for polymer solar cells. Nat. Commun. 9, 743 (2018).
- 16. Cui, Y. et al. Single-junction organic photovoltaic cell with 19% efficiency. *Adv. Mater.* **33**, 2102420 (2021).
- 17. Guan, S. et al. Balancing the selective absorption and photon-toelectron conversion for semitransparent organic photovoltaics with 5.0% light-utilization efficiency. *Adv. Mater.* **34**, 2205844 (2022).
- Kong, W. et al. P-type Polymers in Semitransparent Organic Photovoltaics. Angew. Chem. Int. Ed. 62, e202307622 (2023).
- Liu, W. et al. Theory-guided material design enabling highperformance multifunctional semitransparent organic photovoltaics without optical modulations. Adv. Mater. 34, 2200337 (2022).
- Sun, S. et al. Solution processed semi-transparent organic solar cells over 50% visible transmittance enabled by silver nanowire electrode with sandwich structure. Adv. Mater. 35, 2305092 (2023).
- Xie, D. et al. A 2.20 eV bandgap polymer donor for efficient colorful semitransparent organic solar cells. Adv. Funct. Mater. 33, 2212601 (2023).
- 22. Liu, X., Zhong, Z., Zhu, R., Yu, J. & Li, G. Aperiodic band-pass electrode enables record-performance transparent organic photovoltaics. *Joule* **6**, 1918–1930 (2022).
- 23. Yu, J., Liu, X., Zhou, J. & Li, G. High-performance neutral-color semitransparent organic photovoltaics with optical and thermal management. *Adv. Funct. Mater.* **34**, 2406070 (2024).
- Liu, X. et al. High-performance colorful organic photovoltaics with microcavity resonance color filter. Adv. Energy Mater. 13, 2301361 (2023).
- Liang, N. et al. Trans-reflective structural color filters assisting multifunctional-integrated semitransparent photovoltaic window. Adv. Mater. 35, 2300360 (2023).
- Chen, Y.-H. et al. Microcavity-embedded, colour-tuneable, transparent organic solar cells. Adv. Mater. 26, 1129–1134 (2014).
- 27. Deng, B. et al. The art and science of translucent color organic solar cells. *Nat. Commun.* **16**, 597 (2025).
- Shen, P., Wang, G., Kang, B., Guo, W. & Shen, L. High-efficiency and high-color-rendering-index semitransparent polymer solar cells induced by photonic crystals and surface plasmon resonance. ACS Appl. Mater. Interfaces 10, 6513–6520 (2018).
- 29. Sun, C. et al. Heat-insulating multifunctional semitransparent polymer solar cells. *Joule* **2**, 1816–1826 (2018).
- 30. Wang, D. et al. High-performance and eco-friendly semitransparent organic solar cells for greenhouse applications. *Joule* **5**, 945–957 (2021).
- 31. Pu, J., Han, M., Shen, C., Wang, J. & Lu, L. Constructing a new biomass-based bistatic window for solar regulation. *Adv. Sci.* 11, 2401991 (2024).
- 32. Wheeler, V. M. et al. Photovoltaic windows cut energy use and CO<sub>2</sub> emissions by 40% in highly glazed buildings. *One Earth* **5**, 1271–1285 (2022).
- Ma, W., Yang, C., Gong, X., Lee, K. & Heeger, A. J. Thermally stable, efficient polymer solar cells with nanoscale control of the interpenetrating network morphology. *Adv. Funct. Mater.* 15, 1617–1622 (2005).
- 34. He, Z. et al. Single-junction polymer solar cells with high efficiency and photovoltage. *Nat. Photon.* **9**, 174–179 (2015).
- 35. Qin, J. et al. A chlorinated copolymer donor demonstrates a 18.13% power conversion efficiency. *J. Semicond.* **42**, 010501 (2021).

- Sariciftci, N. S., Smilowitz, L., Heeger, A. J. & Wudl, F. Photoinduced electron transfer from a conducting polymer to buckminsterfullerene. Science 258. 1474–1476 (1992).
- Wienk, M. M. et al. Efficient methano[70]fullerene/MDMO-PPV bulk heterojunction photovoltaic cells. Angew. Chem. Int. Ed. 42, 3371–3375 (2003).
- 38. Li, C. et al. Non-fullerene acceptors with branched side chains and improved molecular packing to exceed 18% efficiency in organic solar cells. *Nat. Energy* **6**, 605–613 (2021).
- Cui, Y. et al. Single-junction organic photovoltaic cells with approaching 18% efficiency. Adv. Mater. 32, 1908205 (2020).
- Jiang, W. et al. π-expanded carbazoles as hole-selective selfassembled monolayers for high-performance perovskite solar cells. Angew. Chem. Int. Ed. 61, e202213560 (2022).
- 41. He, R. et al. Improving interface quality for 1-cm2 all-perovskite tandem solar cells. *Nature* **618**, 80–86 (2023).
- Fu, J. et al. 19.31% binary organic solar cell and low non-radiative recombination enabled by non-monotonic intermediate state transition. *Nat. Commun.* 14, 1760 (2023).
- Zhao, Y. et al. Achieving sustainability of greenhouses by integrating stable semi-transparent organic photovoltaics. *Nat. Sustain.* 6, 539–548 (2023).
- Wang, L. et al. Donor-acceptor mutually diluted heterojunctions for layer-by-layer fabrication of high-performance organic solar cells. Nat. Energy 9, 208–218 (2024).
- Tamai, Y., Murata, Y., Natsuda, S.-i & Sakamoto, Y. How to interpret transient absorption data?: an overview of case studies for application to organic solar cells. Adv. Energy Mater. 14, 2301890 (2024).
- Zeng, R. et al. Achieving 19% efficiency in non-fused ring electron acceptor solar cells via solubility control of donor and acceptor crystallization. Nat. Energy 9, 1117–1128 (2024).
- Liu, S. et al. High-efficiency organic solar cells with low nonradiative recombination loss and low energetic disorder. *Nat. Pho*ton. 14, 300–305 (2020).
- 48. Menke, S. M., Ran, N. A., Bazan, G. C. & Friend, R. H. Understanding energy loss in organic solar cells: toward a new efficiency regime. *Joule* **2**, 25–35 (2018).
- 49. Liu, X., Zhao, Y., Yu, J. & Zhu, R. High-performance bifacial semi-transparent organic photovoltaics featuring a decently transparent TeO2/Ag electrode. *Mater. Chem. Front.* **5**, 8197–8205 (2021).
- 50. Yang, C., Liu, D., Bates, M., Barr, M. C. & Lunt, R. R. How to accurately report transparent solar cells. *Joule* **3**, 1803–1809 (2019).
- Reese, M. O. et al. Consensus stability testing protocols for organic photovoltaic materials and devices. Sol. Energy Mater. Sol. Cells 95, 1253–1267 (2011).
- 52. Khenkin, M. V. et al. Consensus statement for stability assessment and reporting for perovskite photovoltaics based on ISOS procedures. *Nat. Energy* **5**, 35–49 (2020).
- Pu, J., Li, Y., Xu, D., Shen, C. & Lu, L. A quantitative investigation on the cooling benefits of retrofitting building skylights with broadband-spectrum selectivity in China. *Appl. Energy* 381, 125101 (2025).

# Acknowledgements

G.L. gratefully acknowledges the funding from Research Grants Council of Hong Kong (Project Nos. 15221320, 15307922, C4005-22Y), RGC Senior Research Fellowship Scheme (SRFS2223-5S01), the Hong Kong

Polytechnic University: Sir Sze-yuen Chung Endowed Professorship Fund (8-8480), RISE (Q-CDBK), and PRI (1-CD7X). L. L. acknowledges the funding from the Hong Kong Polytechnic University, Projects of RISUD (1-BBG8). C. D. acknowledges the funding from the National Natural Science Foundation of China (22275058), Guangdong Basic and Applied Basic Research Foundation (2022B1515120008), and Guangdong Innovative and Entrepreneurial Research Team Program (2019ZT08L075).

#### **Author contributions**

G.L. and J.Y. conceived the idea and designed the experiments. J.Y. carried out the device fabrication, simulation, and characterization. J.P. and L.L. carried out the simulation on smart windows. D.X. and C.D. synthesized the PBOF. Z. A. carried out the optical simulation. Y.L. and M.C. helped in the characterization and experiment. J.Y. wrote the original draft, and G.L. revised the writing and supervised the project. All authors discussed the results and commented on the manuscript.

### **Competing interests**

The authors declare no competing interests.

#### **Additional information**

**Supplementary information** The online version contains supplementary material available at https://doi.org/10.1038/s41467-025-62546-8.

**Correspondence** and requests for materials should be addressed to Chunhui Duan, Lin Lu or Gang Li.

**Peer review information** *Nature Communications* thanks Xiaozhang Zhu and the other anonymous reviewer(s) for their contribution to the peer review of this work. A peer review file is available.

**Reprints and permissions information** is available at http://www.nature.com/reprints

**Publisher's note** Springer Nature remains neutral with regard to jurisdictional claims in published maps and institutional affiliations.

Open Access This article is licensed under a Creative Commons Attribution-NonCommercial-NoDerivatives 4.0 International License, which permits any non-commercial use, sharing, distribution and reproduction in any medium or format, as long as you give appropriate credit to the original author(s) and the source, provide a link to the Creative Commons licence, and indicate if you modified the licensed material. You do not have permission under this licence to share adapted material derived from this article or parts of it. The images or other third party material in this article are included in the article's Creative Commons licence, unless indicated otherwise in a credit line to the material. If material is not included in the article's Creative Commons licence and your intended use is not permitted by statutory regulation or exceeds the permitted use, you will need to obtain permission directly from the copyright holder. To view a copy of this licence, visit <a href="https://creativecommons.org/licenses/by-nc-nd/4.0/">https://creativecommons.org/licenses/by-nc-nd/4.0/</a>.

© The Author(s) 2025